EDGE ARTICLE

Check for updates

Constructing a dual-protection heterointerface for durable anion exchange membrane seawater electrolysis at ampere-level current density

Yue Xu,[a] Yingjian He, [ID][a] Shuaidong Li,[a] Shanling Li,[b] Junqin Shi,*[b] Zeyun Cai,*[c] Xi Lin*[a] and Kailong Hu [ID] *[ad]

Chloride ions (Cl^-) pose a corrosive challenge to the long-term durability of metal catalysts during seawater electrolysis for sustainable hydrogen production. The construction of heterointerfaces has been demonstrated to enhance the corrosion resistance of highly active transition metals by preventing direct contact with Cl^- in seawater. However, reliance on a single protection mechanism has hindered further advances in heterojunction catalysts. In particular, the charge-transfer regulation induced by the spatial electric field at heterointerfaces has often been overlooked. Herein, we investigate the Cl^- corrosion behavior at the graphene/NiMo interface, which serves as a hydrogen evolution catalyst for durable seawater electrolysis. The spatial electric field formed at the heterointerface promotes the electron density on the graphene surface, thereby suppressing Cl^- accumulation through electrostatic repulsion. Furthermore, doping the graphene layer with a strong electron-accepting element can significantly improve electron transfer and enhance Cl^- resistance. In addition, the formation of C–Cl bonds on the graphene surface inhibits the diffusion of Cl^- toward the metal through a steric effect. N-doped graphene-encapsulated NiMo (NG/NiMo) achieves a current density of 1.0 A cm^{-2} at 1.86 V in an anion exchange membrane (AEM) electrolyzer using seawater as the feedstock, maintaining durability for over 300 h. This work provides new insights into constructing a dual-protection heterointerface by combining electrostatic repulsion and the steric effect to achieve long-term protection for metal catalysts in seawater.

1 Introduction

The utilization of renewable energy-driven water electrolysis represents a clean and scalable approach to produce high-purity hydrogen, effectively addressing the intermittent fluctuations associated with renewable power sources such as solar and wind energies.[1–3] However, this method necessitates a substantial quantity of ultrapure freshwater, which accounts for only 2.5% of global water resources and may exacerbate the prevailing water crisis. In this regard, seawater, constituting approximately 97% of Earth's water resources, emerges as a viable alternative to alleviate the limited availability of

[a]School of Materials Science and Engineering, Institute of Materials Genome & Big Data, Harbin Institute of Technology, Shenzhen 518055, P. R. China. E-mail: hukailong@hit.edu.cn; linxi@hit.edu.cn

[b]State Key Laboratory of Solidification Processing, Center of Advanced Lubrication and Seal Materials, School of Materials Science and Engineering, Northwestern Polytechnical University, Xi'an, Shanxi 710072, P. R. China. E-mail: junqin.shi@nwpu.edu.cn

[c]Institute of Special Environments Physical Sciences, Harbin Institute of Technology, Shenzhen 518055, P. R. China. E-mail: caizeyun@hit.edu.cn

[d]Shenzhen Key Laboratory of New Materials Technology, Harbin Institute of Technology, Shenzhen 518055, Guangdong, P. R. China

freshwater in large-scale applications aimed at sustainable hydrogen production *via* water electrolysis.[4–9] The high concentration of chloride ions (Cl^-, 19 000 mg L^{-1}) in seawater poses significant challenges to the corrosion resistance of electrode catalysts. Cl^- ions tend to adsorb on the surface of metal catalysts ($M + Cl^- \rightarrow MCl_{ads} + e^-$, where M represents the catalyst surface), which thereby triggers the undesired corrosion of metals ($MCl_{ads} + Cl^- \rightarrow MCl_x^-$).[10,11] The corrosion of metals caused by Cl^- ions leads to the deterioration of catalytic performance, posing a significant threat to the long-term durability of electrolyzers.[12,13] Hence, the development of metal catalysts with enhanced corrosion resistance is imperative for achieving environmentally sustainable hydrogen production through electrochemical seawater splitting.

The harsh operation conditions, such as acidic and corrosive electrolytes, require the use of platinum (Pt) group metals as corrosion-proof catalysts for the cathodic hydrogen evolution reaction (HER). However, the scarcity and high cost of Pt-based catalysts pose significant barriers to the large-scale commercialization of hydrogen generation through seawater electrolysis.[14] Non-noble metals are cost-efficient but are susceptible to Cl^--triggered corrosion.[15–17] Recently, interface engineering has emerged as an effective approach to achieve corrosion-resistant

non-noble metal catalysts in seawater electrolysis.[18–24] For example, He *et al.* revealed that CoP possess the function of repelling Cl⁻ *via* theoretical calculations, and thus designed a corrosion-resistant electrode for seawater electrolysis.[9] By constructing a heterojunction that combines CoP with graphene supported on a Ti fiber, the resulting heterojunction catalyst CoP/rGO@Ti exhibits excellent catalytic activity and stability in a salt-rich alkaline electrolyte. The superior durability and activity are attributed to the Cl⁻ repulsion effect on the CoP-coated surface and the charge synergy effect at its interface with rGO. Furthermore, Liu *et al.* reported a corrosion-resistant heterointerface electrocatalyst, consisting of a Ni_4Mo conductive substrate, a $RuO_2/NiOOH$ active phase, and a $NiMoO_4$ anti-corrosion layer.[25] Benefiting from the *in situ* formed MoO_4^{2-} layer, which repels Cl⁻ on its surface, the AEM electrolyzer assembled with this electrocatalyst achieved stable alkaline seawater electrolysis continuously for 240 hours at a current density of 0.5 A cm⁻². However, the corrosion resistance of most heterointerface catalysts in seawater electrolysis is still limited to a single repulsion mechanism. In particular, the effect of the spatial electric field spontaneously generated inside the heterojunction has been overlooked in this process. Therefore, it is particularly important to thoroughly explore the multiple action mechanisms of Cl⁻ corrosion-resistant heterojunction catalysts.

In this work, we propose an effective resistant strategy for Cl⁻ corrosion by constructing a dual-protection heterointerface consisting of a N-doped graphene layer and a highly active NiMo alloy (NG/NiMo). This architecture enables efficient and stable seawater electrocatalysis under ampere-level harsh conditions. Molecular dynamics (MD) simulations and density functional theory (DFT) calculations suggest that the strong electron acceptor N enhances the spatial electric field at the NG/NiMo heterointerface, accelerating interfacial charge transfer. This process facilitates partial electron enrichment on the NG surface, thereby inhibiting the diffusion of Cl⁻ and resulting in an eleven-fold decrease in the catalyst–Cl⁻ interaction energy. Furthermore, the formation of C–Cl bonds effectively prevents Cl⁻ from bonding with metal surfaces through a steric effect, thereby suppressing metal dissolution. In combination with the electrostatic repulsion and steric effect, a three-fold decline in elemental dissolution is achieved for NG/NiMo in comparison to bare NiMo after 100 h of seawater electrolysis. This work provides novel insights for the design of efficient and durable non-noble metal catalysts for hydrogen production from seawater electrolysis.

2 Results and discussion

2.1 The heterointerface electric field effect and theoretical calculations

The adsorption behaviors of Cl⁻ ions on the catalyst surface in the simulated seawater environments were investigated through MD simulations and DFT calculations. The equilibrium configurations of certain species (Na⁺, Cl⁻, and H_2O) in seawater above the surface of bare NiMo, the dual-protection heterointerface model composed of pristine graphene (G/NiMo)

and N-doped graphene (NG/NiMo) are displayed in Fig. 1a and Table S1. The densities of Cl⁻ ions were plotted as a function of the distance between the ions and the catalyst surface (Fig. 1b). The accumulated Cl⁻ ions above NG/NiMo exhibit a location distance of 0.38 nm, which is farther than those located on the surface of NiMo (0.25 nm) and G/NiMo (0.32 nm). Furthermore, the quantities of Cl⁻ ions within a 5 Å distance above the surfaces of NiMo, G/NiMo, and NG/NiMo were counted at the equilibrium state of the simulation (Fig. 1c). Bare NiMo exhibits an approximate Cl⁻ amount of 0.12 mol m⁻², whereas NG/NiMo displays half that quantity. These results demonstrate that NG/NiMo exhibits the most pronounced repulsion towards Cl⁻ ions. The MD simulation also considered the quantities of H_2O molecules within 10 Å above the surfaces of NiMo, G/NiMo, and NG/NiMo. Notably, both G/NiMo and NG/NiMo surfaces exhibit a higher abundance of H_2O molecules compared to the NiMo surface, suggesting that the establishment of the heterointerface enhances the adsorption capacity for H_2O molecules (Fig. S1).

The mean square displacement in the Z direction (MSD-Z) was extracted to elucidate the diffusion characteristics of Cl⁻ ions on the three systems (*i.e.*, NiMo, G/NiMo, and NG/NiMo).[26] The MSD-Z value reaches a stable state within 0.1 ns, suggesting that the adsorption or repulsion process of ions/molecules on the catalyst surface occurs at an ultrafast rate (Fig. S2). The MSD-Z value of Cl⁻ ions on the NG/NiMo surface shows the highest magnitude, followed by the bare NiMo surface, whereas the G/NiMo surface presents the lowest value. These results can be ascribed to the robust electrostatic attraction between Cl⁻ ions and the bare NiMo surface, as well as the pronounced repulsive forces exerted by Cl⁻ ions on the NG/NiMo surface. In contrast, the G/NiMo surface exhibits a moderate interaction with Cl⁻ ions, resulting in the weakest diffusion behavior. After achieving equilibrium in the simulated system, the calculation of interaction energy between Cl⁻ ions and the surface was conducted (Fig. 1d). The interaction energy between NiMo and Cl⁻ (NiMo–Cl⁻) is 28.0 kcal mol⁻¹, which exceeds eleven-fold the value observed for NG/NiMo–Cl⁻ (2.4 kcal mol⁻¹). NG/NiMo–Cl⁻ also demonstrates an interaction energy value three times smaller than that of G/NiMo–Cl⁻ in comparison. Therefore, constructing an interface composed of N-doped graphene significantly enhances the repulsion effect towards Cl⁻ ions, thereby demonstrating great potential for facilitating a sustainable seawater electrolysis process.

To further clarify the underlying mechanisms responsible for the Cl⁻ ion repulsive phenomenon of NG/NiMo, DFT calculations were carried to examine the roles of the heterointerface and N doping in Cl⁻ ion repulsion under seawater conditions. The DFT models of G/NiMo and NG/NiMo are shown in Fig. S3. The charge density differences along the Z-axis are illustrated at the graphene/NiMo interfaces for the G/NiMo and NG/NiMo models (Fig. 1e). The numbers of electrons transferred from the NiMo substrate toward graphene and N-doped graphene are calculated to be 0.59 and 1.48 e for G/NiMo and NG/NiMo, respectively. The high electronegativity of N dopants contributes to the formation of enhanced spatial electric fields, which promote electron transfer from NiMo to
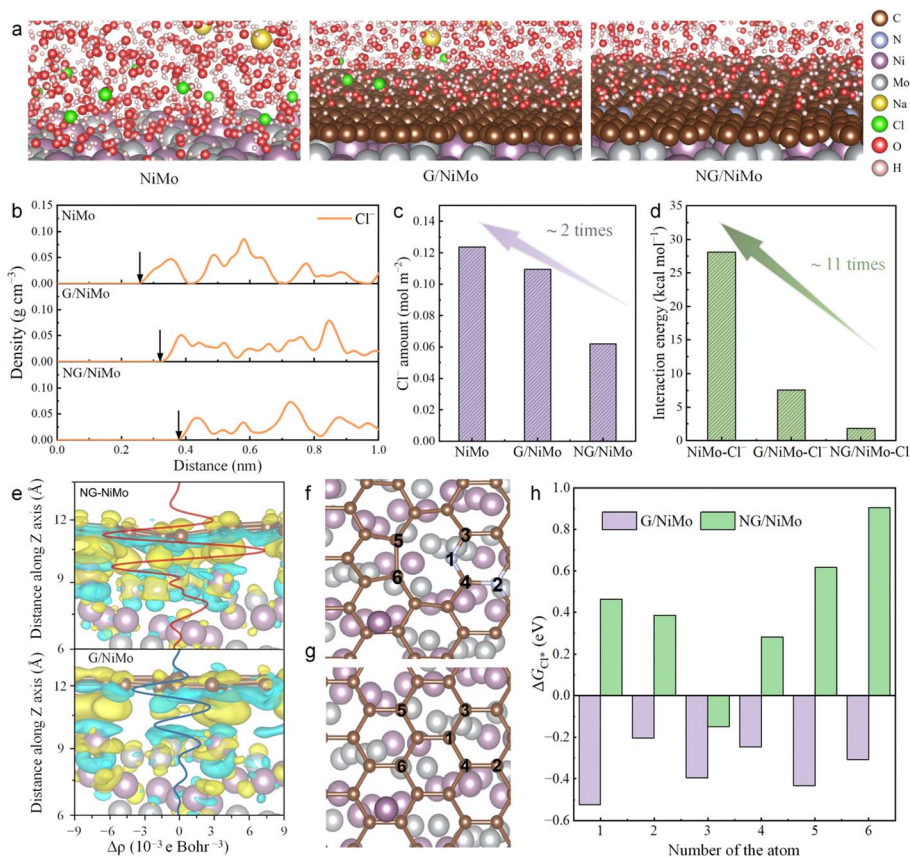
Fig. 1 Theoretical calculations. (a) Equilibrium configurations of NiMo, G/NiMo and NG/NiMo models in a simulated seawater environment. (b) The mass densities of Cl⁻ ions *versus* distance above the NiMo, G/NiMo, and NG/NiMo surfaces. (c) The quantities of Cl⁻ ions located within a 5 Å distance above the surfaces of NiMo, G/NiMo, and NG/NiMo. (d) Interaction energy between Cl⁻ and the NiMo, G/NiMo, and NG/NiMo surfaces. (e) The electron transfer and distribution at the interface in G/NiMo and NG/NiMo. The top view of (f) G/NiMo and (g) NG/NiMo models with marked certain atoms for ΔG_{Cl*} calculations. (h) The calculated ΔG_{Cl*} values of the certain atoms in (f) and (g).

the graphene layer, ultimately leading to surface electron enrichment. The effect of the electron-rich state of N-doped graphene on the adsorption behavior of Cl⁻ ions was further examined based on the Gibbs free energy of Cl adsorption (ΔG_{Cl*}). Six atoms on the graphene and N-doped graphene surfaces were selected as the potential adsorption sites for further analysis (Fig. 1f and g). As shown in Fig. 1h, all six atom sites on the pure graphene surface in G/NiMo demonstrate ΔG_{Cl*} values ranging between −0.52 and −0.2 eV, indicating strong adsorption of Cl on the graphene surface. In a sharp contrast, NG/NiMo exhibits positive ΔG_{Cl*} values, ranging from +0.28 to +0.89 eV, in most cases. The large positive ΔG_{Cl*} values indicate a strong repulsion effect of Cl⁻. The disparity in the ΔG_{Cl*} of G/NiMo and NG/NiMo can be attributed to the strong spatial electric field effect induced by N doping, which acts as a strong electron acceptor. This effect enhances electron transfer from NiMo to the graphene, thereby regulating electron enrichment at the surface and ultimately strengthening the repulsive force against Cl⁻ ions.

2.2 Sample preparation and characterization

According to the results obtained from the above theoretical calculations, the N-doped graphene layer contributes to

effective protection against Cl⁻-induced corrosion in seawater. Through integrating the enhanced spatial electric field caused by negatively charged N dopants and the accompanying electron enrichment effect at the surface, the efficient and durable seawater reduction can be achieved by constructing hetero-interfaces between N-doped graphene and a highly active NiMo catalyst (Fig. 2a). The bare NiMo alloy was synthesized through a typical hydrothermal method and thermal reduction treatment.[27] The graphene layer deposition was achieved by a chemical vapor deposition (CVD) process.[28,29] Benzene and pyridine were used as the precursors to grow graphene and N-doped graphene on the NiMo surface, abbreviated as G/NiMo and NG/NiMo. The NiMo alloy shows a bicontinuous and open porous morphology, with pore sizes of a few hundred nanometers (Fig. 2b, c, S4 and S5). High-resolution transmission electron microscopy (HRTEM) imaging reveals the graphene/NiMo interface in NG/NiMo, showing a graphene layer thickness of less than 2 nm (Fig. 2d). The fast Fourier transform (FFT) images show sharp diffraction spots in the regions of the NiMo substrate (Fig. 2e) and graphene layers (Fig. 2f), indicating their high crystallinity. The atomic-resolution TEM images demonstrate the NiMo alloy with a lattice distance of 2.07 Å, assigned to the (313) plane (Fig. 2g and h). The lattice distance
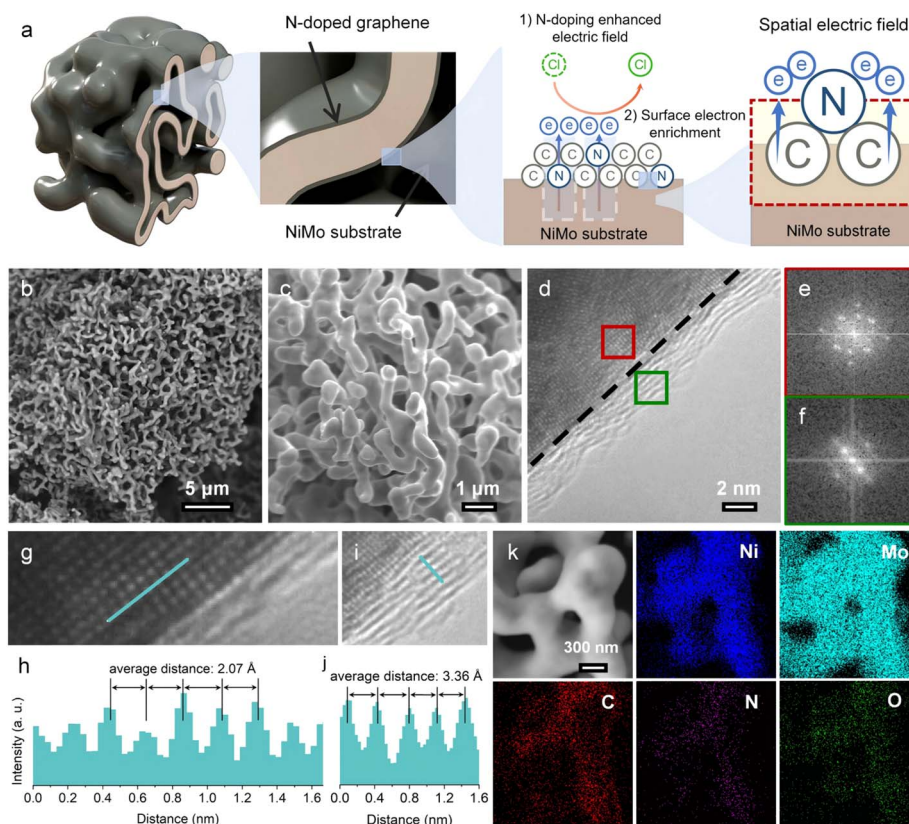
Fig. 2 Morphological characterization. (a) Schematic illustration of the structure of the NG/NiMo electrocatalyst and the corrosion-resistant mechanism. (b and c) SEM images of the as-prepared NG/NiMo sample. (d) TEM image of the heterointerface. (e and f) FFT images of the selected area highlighted by red marks (NiMo) and green marks (NG) in (d). (g) TEM image of NiMo and the (h) corresponding line profile of the intensity marked by the cyan line in (g). (i) TEM image of graphene and the (j) corresponding line profile of the intensity marked by the cyan line in (i). (k) EDS elemental mapping of the NG/NiMo sample.

of graphene is 3.36 Å, corresponding to the (002) plane of graphite (Fig. 2i and j). Energy dispersive spectroscopy (EDS) mapping confirms that the porous sample is composed of Ni, Mo, C, and N elements with a uniform distribution (Fig. 2k).

The structural characterization studies of the as-prepared samples were carried out by X-ray diffraction (XRD) and Raman spectroscopy. XRD patterns of NiMo, G/NiMo, and NG/NiMo show a dominant peak located at 43.8°, corresponding to the (313) plane of NiMo (JCPDS No. 48-1745) (Fig. S6). G/NiMo and NG/NiMo samples exhibit the typical Raman spectra of multi-layer graphene with heteroatomic dopants (Fig. S7). The intensity ratio of the D to G band (I_D/I_G) in NG/NiMo is 1.19, exceeding that observed for G/NiMo ($I_D/I_G = 0.57$). The large I_D/I_G value suggests the high topological defect density of graphene layers in NG/NiMo, owing to the introduction of N dopants.[30] Besides, the comparable 2D/G band intensity ratio indicates that NG/NiMo and G/NiMo possess graphene layers with similar thickness.

The binding states and quantitative chemical compositions of the samples were investigated by X-ray photoelectron spectroscopy (XPS). The high-resolution Ni 2p spectra of NiMo, G/NiMo, and NG/NiMo comprise major peaks at 852.9 and 856.0 eV that are assigned to Ni^0 $2p_{3/2}$ and Ni^{2+} $2p_{3/2}$ (Fig. S8a, S9a and S10a).[31] The two additional peaks at 859.0 and 862.0 eV are the

relevant satellite peaks.[32] The Mo 3d spectra are deconvoluted into dominant Mo^0 (227.9 and 231.1 eV) peaks, with certain contributions of Mo^{4+} (229.0 and 232.1 eV), Mo^{5+} (230.6 and 233.7 eV) and Mo^{6+} (232.3 and 235.4 eV) peaks (Fig. S8b, S9b and S10b).[33] In the case of NG/NiMo, the typical C 1s XPS spectrum shows peaks at 284.8, 286.6, and 288.9 eV, corresponding to C–C, C–O–C, and O–C=O bonds, respectively (Fig. S10c).[34] For the N 1s XPS spectrum, the main peak at 397.9 eV is ascribed to pyridinic N species, whereas the other peak at 395.9 eV is assigned to the Mo–N bond (Fig. S10d).[35,36] Additionally, the Mo 3p (394.0 eV) peak is also detected for NG/NiMo. The presence of N dopants on the graphene layers of NG/NiMo is confirmed through XPS, with a N content of 8.15 at%.

2.3 Electrocatalytic performances in seawater

The electrocatalytic performances of the as-synthesized electrocatalysts were evaluated by using a three-electrode cell in simulated seawater (pH ≈ 8.0). The intrinsic HER activity was investigated by normalizing the polarization curves with the electrochemically active surface area (ECSA) (Fig. S11 and S12).[37] NG/NiMo exhibits a HER performance comparable to that of commercial 20 wt% Pt/C in seawater. Tafel plots reveal that the corrosion potentials (E_{corr}) of NiMo, G/NiMo, and NG/NiMo are 140, 223, 252 mV vs. RHE, respectively (Fig. 3a). Notably, the

corrosion potential of NG/NiMo is more positive than those of NiMo and G/NiMo in seawater, indicating a lower tendency for corrosion and superior corrosion resistance compared to NiMo, and G/NiMo.[25,38] Furthermore, the breakdown potential (E_b) and pitting potential (E_{pit}) of each sample are clearly labeled as key metrics for the quantitative evaluation of corrosion resistance. NG/NiMo exhibits the highest E_b and E_{pit} values. This result confirms that NG/NiMo displays superior breakdown resistance, pitting corrosion resistance, and structural stability in Cl^--containing environments. Furthermore, when compared with other reported electrocatalysts, NG/NiMo demonstrates a remarkably low corrosion current density (I_{corr}) at a relatively high E_{corr} (Fig. 3b and Table S5). Electrochemical impedance spectroscopy (EIS) was further employed to understand the charge transfer property (Fig. S13). The bare NiMo alloy displays the fastest charge transfer while the graphene layer deposition slightly increases the charge-transfer resistance.

Long-term durability is significant to assess the catalytic performance in seawater electrolysis. Chronoamperometry (CA) measurement was carried out at a consistent working potential of −0.6 V *vs.* RHE for commercial 20 wt% Pt/C, NiMo, and NG/NiMo (without *iR* compensation). NG/NiMo retains 95.3% of the initial current density after a 300 h CA test (Fig. S14). In comparison, only 62.8% of its initial current density is retained for NiMo. The commercial 20 wt% Pt/C drops dramatically to 52.6% of its beginning activity within 20 h. These results show that Pt/C and bare NiMo suffer intense corrosion in seawater, while the establishment of NG/NiMo heterointerfaces successfully improves durability. Inductively coupled plasma-mass spectroscopy (ICP-MS) analyses demonstrate the dissolution ratios of Mo and Ni during a 100 h CA test (Fig. 3c). NiMo suffers severe elemental dissolution with $22.5 \pm 0.5\%$ and $7.1 \pm 0.2\%$ for Mo and Ni. By comparing the dissolution behaviors of NiMo and G/NiMo, graphene layer deposition is shown to slightly mitigate dissolution. In contrast, NG/NiMo demonstrates small dissolution ratios of Ni ($2.3 \pm 0.1\%$) and Mo ($7.3 \pm 0.3\%$), representing a three-fold decline in elemental dissolution compared to NiMo. Notably, no further increase is observed for the Ni/Mo dissolution ratio after 10 and 50 h tests, suggesting the long-term corrosion resistance of NG/NiMo.

The practical application of catalysts for overall electrolysis in seawater was evaluated using an anion exchange membrane (AEM) electrolyzer. An AEM electrolyzer was assembled by using as-synthesized NiMo samples and commercial IrO$_2$ as cathode and anode catalysts (Fig. 3d and e). The polarization curves of NiMo, G/NiMo, NG/NiMo, and 20 wt% Pt/C assembled AEM electrolyzers were measured at 60 °C. The electrolyzer assembled with NG/NiMo as the cathode catalyst requires a cell voltage of only 1.86 V to reach a current density of 1.0 A cm^{-2}, whereas the counterparts employing NiMo and G/NiMo as cathode catalysts exhibit cell voltages of 1.99 V and 2.18 V, respectively (Fig. 3f). In addition, the performance of the NG/
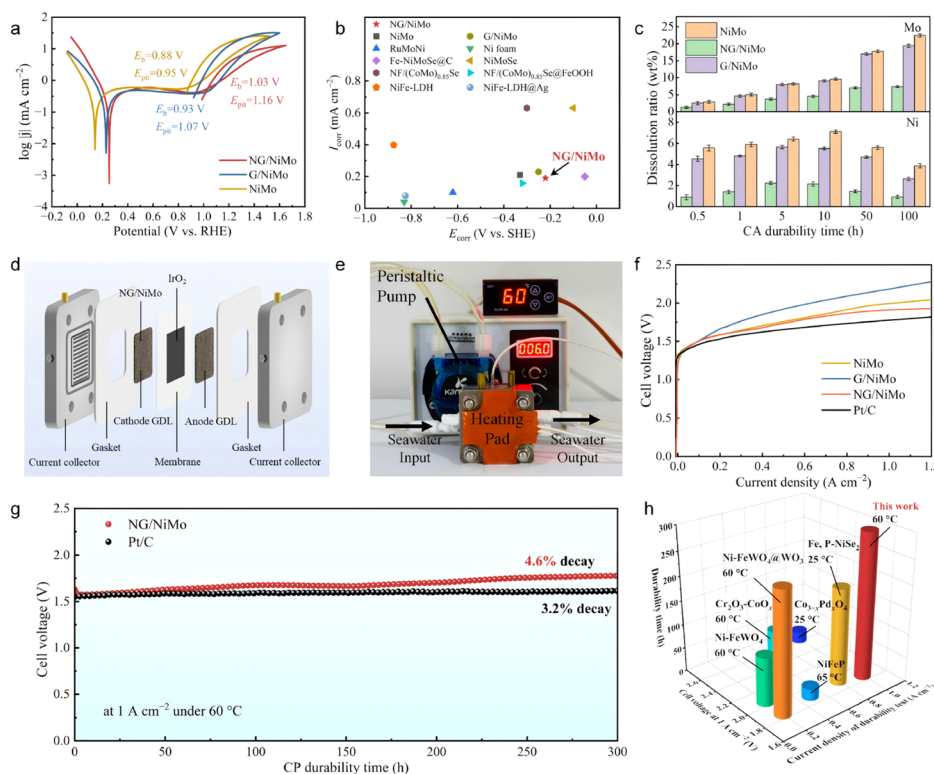

Fig. 3 Electrocatalytic performances in simulated seawater (pH ≈ 8). (a) Tafel plots of NiMo, NG/NiMo, and G/NiMo. (b) Comparison of corrosion parameters of various reported electrocatalysts in seawater. (c) Dissolution ratios of Ni and Mo for NiMo, NG/NiMo, and G/NiMo during 100 h of continuous electrolysis. (d) Schematic diagram of the AEM electrolyzer components. (e) Photograph of the AEM cell setup. (f) Polarization curves of electrolyzers with NiMo, G/NiMo, NG/NiMo, and Pt/C as cathodes. (g) Durability test of the NG/NiMo and 20 wt% Pt/C-assembled AEM electrolyzers at 1.0 A cm^{-2}. (h) Comparison of the performance of AEM electrolyzers with various cathode catalysts.

NiMo-catalyzed AEM electrolyzer is comparable to that of the electrolyzer catalyzed by commercial 20 wt% Pt/C. Furthermore, to assess the durability of the AEM cell assembled with NG/NiMo and commercial 20 wt% Pt/C, a chronopotentiometry (CP) test was conducted at 1.0 A cm^{-2} and 60 °C. The NG/NiMo assembled AEM electrolyzer can operate for over 300 h with a performance degradation rate of less than 5.0% (Fig. 3g), exhibiting stability comparable to commercial 20 wt% Pt/C (3.2% decay). The slight degradation of the NG/NiMo assembled AEM electrolyzer arose from the corrosion and removal of IrO$_2$ on the anode side. However, Cl$^-$ inevitably induce corrosion of NG/NiMo, resulting in a further degradation of catalytic performance compared to standard commercial electrodes. To provide a comprehensive evaluation of NG/NiMo-enabled AEM seawater electrolysis, its performance was compared with other state-of-the-art catalysts reported in the literature.[39–43] As illustrated in Fig. 3h, NG/NiMo exhibits superior AEM cell performance relative to recently reported non-noble metal catalysts under seawater conditions (Table S6). The above results demonstrate that NG/NiMo achieves Pt/C-comparable activity and exceptional durability in AEM-based seawater electrolysis, positioning it as a highly promising candidate for large-scale hydrogen production.

2.4 The surface chemical states and corrosion behaviors of samples

To investigate the mechanism underlying the superior durability of NG/NiMo during seawater reduction, the surface chemical states of the samples in seawater were analyzed. The samples were immersed in seawater for 5 h to ensure complete interaction between Cl$^-$ ions and the sample surface, subsequently enabling their detection through Raman spectroscopy, FTIR, and XPS. The characteristic peaks at approximate 192 and 217 cm^{-1}, attributed to the presence of Ni–Cl bonds, are observed in both NiMo and G/NiMo (Fig. 4a and S15). Indeed, this Ni–Cl bond is not detected for NG/NiMo, suggesting that the N-doped graphene resists Cl$^-$ diffusion to the NiMo surface. Raman results provide evidence that the corrosion is initiated by Cl$^-$ adsorption on the metal surface, while the N-doped graphene layer effectively prevents the formation of Ni–Cl bonds through efficient repulsion of Cl$^-$ ions. Similar results are also observed for the Mo–Cl bond. FTIR spectra confirm that Cl$^-$ ions are bound with carbon sites on graphene layers to form the C–Cl bond (Fig. 4b),[44] and the resulting steric effect effectively impedes the diffusion of Cl$^-$ ions from the electrolyte to the metallic active sites. The FTIR and Raman results reveal the formation of C–Cl bonds, which effectively retard or even prevent metal–Cl bonding interactions. The characteristic peak at 198.3 eV corresponds to Cl–Mo bonding introduced by the formation of surface metal chlorides.[45] The decrease in the XPS intensity indicates that the content of metal chlorides formed on the surface is significantly reduced (Fig. 4c). This means that NG/NiMo exhibits the lowest amount and accumulation of metal chlorides on its surface, showing the strongest Cl$^-$ repulsion capability.

High-resolution XPS spectra of NiMo, G/NiMo, and NG/NiMo before and after CA measurements were measured to understand the variation of chemical valence states on the sample surface during seawater electrolysis. A sharp decline of the main peaks at 227.9 eV (Mo^0 3d$_{5/2}$) and 231.1 eV (Mo^0 3d$_{3/2}$) is observed for bare NiMo, indicating that severe oxidation of the Mo element resulted from Cl$^-$ adsorption (Fig. S16). In the case of G/NiMo, the Mo 3d spectra show a moderate reduction of Mo^0 and Mo^{4+} peaks, demonstrating minor oxidation compared to NiMo. In contrast, metallic Mo is well preserved and retained most of its initial states after CA tests. High-resolution Ni 2p spectra were also measured (Fig. S17). The variation of the Ni^0 peak with increasing CA time generally shows the same trend as the Mo^0 peaks, but with more drastic oxidation. The Ni^0 peak of G/NiMo retains more than that of NiMo under the same electrolysis time. Although NG/NiMo shows the Ni^0 peak was partially reduced in the initial 2 h, the peak remains nearly the same after the whole CA measurement.

Through the comparison of XPS results before and after CA tests, NG/NiMo demonstrates superior stability in terms of surface chemical compositions compared to NiMo and G/NiMo. To quantitatively analyze the chemical states, the valence ratios of each element were further determined (Tables S2–S4). The metallic ratio of Mo in NiMo decreases from 47.9 to 13.5 at% after an initial 2 h test and subsequently continues to decrease to 5.5 at% after a 5 h CA measurement (Fig. S18). In comparison, G/NiMo presents metallic Mo ratios of 25.4 and 19.1 at% after 2 and 5 h tests, indicating that the graphene layer improves the corrosion resistance against seawater. Notably, the metallic Mo ratio remains as high as 36.9 at% in NG/NiMo during continuous CA testing. The valence variation of the Mo element for NiMo, G/NiMo, and NG/NiMo is shown in Fig. S19. For NiMo, a majority (more than 88.0 at%) of the Mo^0, Mo^{4+}, and Mo^{5+} peaks are oxidized into Mo^{6+}. On the other hand, G/NiMo and NG/NiMo exhibit moderate (60.0 at%) and minor (41.5 at%) oxidation levels with respect to Mo^{6+} ratios. The metallic Ni ratios exhibit a similar trend to that of Mo. Severe corrosion results in a significant decrease in the metallic Ni ratio of NiMo, reaching as low as 10.5% after a 5 h CA test, whereas NG/NiMo retains a substantial amount of metallic Ni at 31.0 at%. This three-fold higher content of metallic Ni indicates enhanced corrosion resistance for NG/NiMo. Overall, NiMo exhibits the highest oxidation states on the sample surface, while NG/NiMo shows the lowest oxidation level and G/NiMo falls in between. The high metal oxidation states exhibited by NiMo and G/NiMo samples are attributed to the formation of metal chlorides on their surfaces. This is in good agreement with the increased content of Cl–Mo bonding in Fig. 4c, confirming the strong interaction between the metallic active layers and Cl$^-$ in NiMo and G/NiMo samples, which further induces significant material corrosion, ultimately leading to a noticeable degradation in the catalytic activity of the samples.

By integrating the results from Raman, FTIR, and XPS analyses of the surface chemical states, a comprehensive elucidation of the corrosion processes occurring on the catalyst surface is presented. The metals sites on the bare NiMo alloy are directly exposed to massive Cl$^-$ ions in seawater, resulting in severe metal dissolution and serious corrosion (Fig. 4d). The presence of a graphene layer leads to the formation of C–Cl
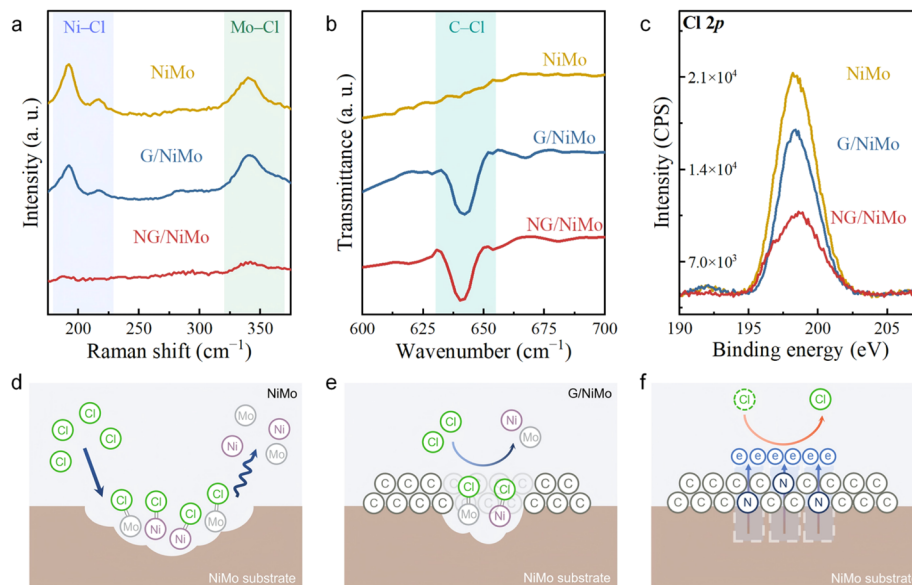
Fig. 4 The surface chemical states and corrosion behaviors of the samples. (a) Raman, (b) FTIR, and (c) XPS Cl 2p spectra of the NiMo, G/NiMo, and NG/NiMo samples immersed in seawater for 5 h. Schematic illustration of the corrosion behaviors and resistance mechanisms for (d) NiMo, (e) G/NiMo, and (f) NG/NiMo samples during seawater electrolysis.

bonds on the C sites, thereby impeding the diffusion of Cl⁻ from the electrolyte to the metal sites through a steric effect. Despite the graphene layer providing protection for the NiMo substrate, some penetration of Cl⁻ ions through the graphene still occurs, giving rise to moderate corrosion of NiMo (Fig. 4e). This arises from the weak spatial electric field between pure graphene and the NiMo alloy, leading to a slow charge separation and consequently insufficient Cl⁻ repulsion driving force. Relatively, in NG/NiMo, the synergistic effect of the spatial electric field from the strong electron acceptor N, endows the material with the strongest Cl⁻ repulsion capability. This integration of the enhanced spatial electric field and the metal protection introduced by the steric effect results in superior corrosion resistance for NG/NiMo during seawater electrolysis (Fig. 4f).

2.5 The corrosion-resistance mechanism

The structure and morphology of the samples after HER tests were characterized by using XRD, Raman, SEM, and TEM measurements. XRD patterns reveal no discernible alteration in the physical phase of NG/NiMo after 2000 CV cycles (Fig. S20). A slight increase is observed in the I_D/I_G value for NG/NiMo, while the I_{2D}/I_G value remains unaltered, suggesting the induction of certain structural defects during the electrocatalytic process (Fig. S21). In contrast, the I_D/I_G ratio of the G/NiMo sample increases significantly, with a variation of 0.15, reflecting a substantial increase of defects (Fig. S22), which further confirms that N doping can effectively stabilize the graphene structure and alleviate Cl⁻-induced defect generation. Both XRD and Raman results validate the exceptional corrosion resistance exhibited by NG/NiMo in seawater. SEM and STEM images demonstrate that the presence of potholes on the surface of NiMo after testing, indicating severe corrosion

(Fig. 5a, b and S23). In contrast, the surface morphology of NG/NiMo remains well-preserved due to the interaction between the N-doped graphene layer and the NiMo substrate (Fig. 5c).

To assess the impact of surface corrosion on the seawater reduction process, EIS measurements were employed at various CA durability test times. Nyquist plots obtained for NiMo exhibit a substantial increase in the size of semi-circles as the test progresses (Fig. 5d), indicating that surface corrosion significantly impedes charge transfer between the catalyst and electrolyte. In contrast, NG/NiMo demonstrates excellent corrosion resistance, resulting in a durable state of surface morphology and chemical composition, as evidenced by stable Nyquist plots recorded during the 1 to 20 h testing period (Fig. 5e). Nyquist plots are further fitted to determine R_{ct} values. The R_{ct} values for NiMo, measured at CA times ranging from 1 to 20 h, are observed to increase continuously with values of 19.2, 28.8, 43.3, and 46.2 Ω, respectively (Fig. 5f). Similarly, EIS tests conducted on NG/NiMo exhibit stable R_{ct} values beyond 5 h with measurements of 11.2, 17.2, 17.4, and 18.2 Ω. In addition, the rate of change in R_{ct} (ΔR_{ct}) was calculated to evaluate the progression of surface corrosion. NiMo exhibits a rapid increase in ΔR_{ct} values within 20 h (Fig. 5g). The continuous augmentation in R_{ct} signifies the persistent corrosion occurring on the catalyst surface. Conversely, NG/NiMo exhibits negligible and stable ΔR_{ct} values after an initial 5 h test, showcasing its resistance to corrosion under uninterrupted operating conditions.

The corrosion resistance of the catalysts can be evaluated by quantifying the energy barriers of elemental dissolution during seawater reduction.[46] The dissolution amounts of Ni and Mo elements in seawater were measured for NiMo, G/NiMo, and NG/NiMo by using the ICP-MS technique. Furthermore, the dissolution rates were determined by plotting the amount of
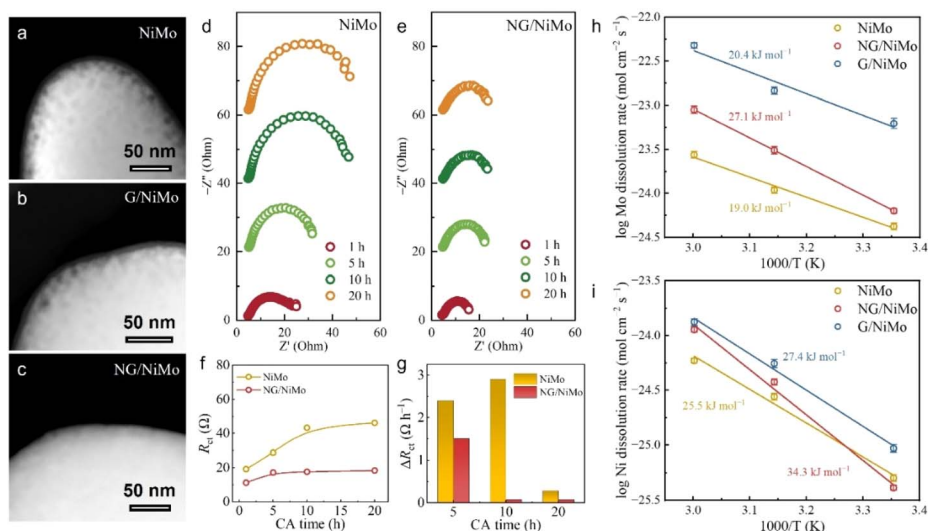
Fig. 5 The surface corrosion analyses of the samples. TEM images of (a) NiMo, (b) G/NiMo, and (c) NG/NiMo samples after a 2000-cycle CV test. (d and e) Electrochemical impedance spectra of NiMo and NG/NiMo after CA tests at various times. (f and g) The charge transfer resistance and the changing-rate of NiMo, and NG/NiMo. (h and i) The metal dissolution rate of NiMo, G/NiMo, and NG/NiMo as a function of temperature.

metal dissolved against CA test times (Fig. S24). The activation energy of the corrosion reaction was obtained by fitting Arrhenius-type plots of the logarithmic dissolution rates as a function of $1000/T$.[47] The activation energies of Mo dissolution are determined to be 19.0, 20.4, and 27.1 kJ mol^{-1} for NiMo, G/NiMo, and NG/NiMo, respectively (Fig. 5h). In addition, the activation energies of Ni dissolution for NiMo, G/NiMo, and NG/NiMo are found to be 25.5, 27.4, and 34.3 kJ mol^{-1} (Fig. 5i). The occurrence of the electrochemical reaction is generally hindered by high activation energy. Experimental results demonstrate that the interface combination of the graphene layer and NiMo can significantly elevate the activation energy, and further enhancement in activation energy can be achieved by introducing N dopants into the graphene. The activation energy results exhibit remarkable consistency with the observed alterations in chemical states on the catalyst surface, as elucidated by XPS, Raman, FTIR, and TEM analyses.

By integrating experimental findings with computational data, we propose a corrosion-resistance mechanism of the heterointerface and analyze the role of N dopants in enhancing Cl$^-$-proof properties during seawater reduction. Three catalyst systems are examined, including the bare NiMo alloy, pure graphene/NiMo alloy interface and N-doped graphene/NiMo interface. In the case of the bare NiMo alloy, Cl$^-$ ions in seawater directly adsorb onto its surface and subsequently initiate the formation of metal chlorides, leading to leaching of Ni and Mo (Fig. 6a). The extensive dissolution of metals and surface oxidation of NiMo are verified through ICP, SEM, TEM, and XPS analyses. This corrosion induced by Cl$^-$ further results in the degradation of electrocatalytic performances during the seawater reduction process. MD simulations reveal a strong interaction energy as high as 28.0 kcal mol^{-1} between the NiMo surface and Cl$^-$ ions (Fig. 1d), resulting in significant accumulation of Cl$^-$ on the surface that promotes continuous corrosion.

When the heterointerface forms between the NiMo alloy and pure graphene, the spatial electric fields of relatively weak strength are generated, accompanied by the formation of C–Cl bonds. The graphene layer dramatically reduces the catalyst–Cl$^-$ interaction compared to bare NiMo, as confirmed by MD and XPS data (Fig. 1d and 4c). Although the direct interaction of NiMo with Cl$^-$ is partially blocked by the graphene barrier, some Cl$^-$ ions can still penetrate through pure graphene layers and adsorb onto the surface of NiMo (Fig. 4a). This means that undoped pure graphene partially impedes the diffusion of Cl$^-$ ions toward NiMo. Indeed, G/NiMo still exhibits severe metal leaching during seawater reduction, including more than 18.0 wt% of Mo and 5.5 wt% of Ni (Fig. 3c). This corrosion observed in G/NiMo may be attributed to a single Cl$^-$ repulsion mechanism. Although C–Cl bonding provides partial protection, the weak spatial electric field results in an inadequate driving force for Cl$^-$ repulsion. Take these results together, we conclude that the pure graphene layer offers protection through a weak spatial electric field and the formation of C–Cl bonds; however, its effectiveness in preventing persistent leaching of metal catalysts in seawater is limited (Fig. 6b).

Once N dopants are introduced into graphene layers, the electronic states on graphene undergo accelerated redistribution, thereby inducing an enhanced spatial electric field. Owing to this electron accelerated redistribution, electrons automatically migrate toward the NG surface, resulting in a surface electron enrichment effect. DFT calculations demonstrate that this electron accumulation state is advantageous for repelling Cl$^-$ ions, as evidenced by ΔG_{Cl*} values (Fig. 1h). A positive ΔG_{Cl*} value represents that the adsorption process of Cl is thermodynamically unfavorable.[22,48] MD simulations further confirm a remarkable eleven-fold decrease in catalyst–Cl$^-$ interaction energy (Fig. 1d). Furthermore, the prominent characteristic peak of C–Cl bonds observed in the FTIR results (Fig. 4b) indicates that Cl$^-$ also preferentially form bonds with C on the
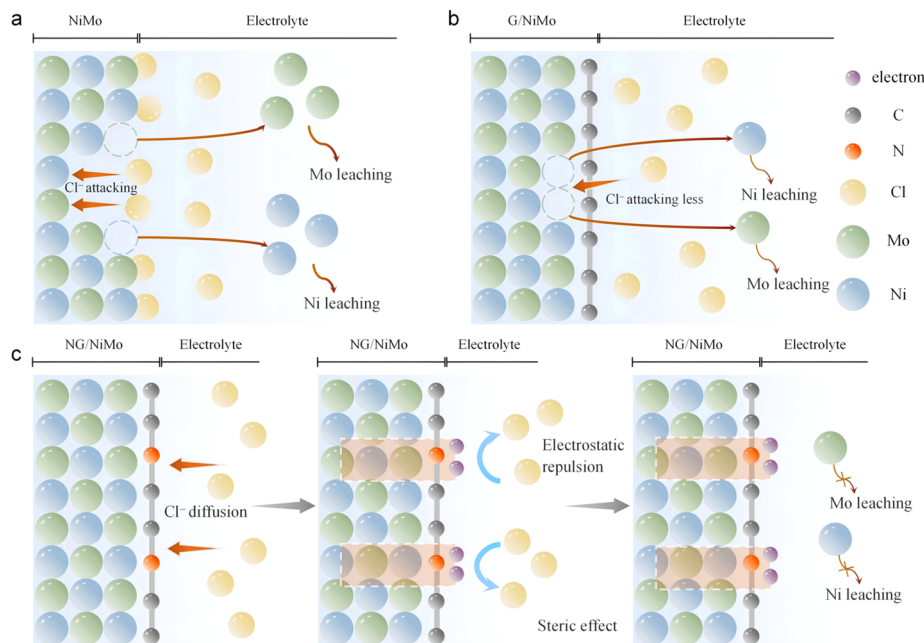
Fig. 6 Schematic corrosion-resistant mechanisms of the dual-protection heterointerface. (a) Cl⁻-induced corrosion occurring on the bare NiMo surface. The strong NiMo–Cl⁻ interaction triggers the persistent leaching of Ni and Mo. The corrosion-resistance mechanism of the heterointerface combining the NiMo alloy with (b) pure graphene and (c) N-doped graphene. G/NiMo provides limited protection against Cl⁻ solely through the steric effect. NG/NiMo effectively repels Cl⁻ by integrating the enhanced spatial electric field and steric effect.

NG surface. The Raman and XPS data for NG/NiMo reveal weak metal–Cl bonding alongside the preservation of the majority of metal valence states, which suggests effective protection of Ni and Mo species (Fig. 4a, S16 and S17). Experimental data corroborate these theoretical findings, revealing exceptional seawater reduction durability exceeding 300 h for NG/NiMo and a sharp significant reduction in metal dissolution (Fig. S14 and 3c). The activity energies associated with Ni and Mo dissolution during electrocatalytic processes provide additional evidence supporting the corrosion resistance imparted by hetero-interface establishment (Fig. 5h and i). Thus, we unveil the corrosion-resistant mechanism of NG/NiMo as a synergistic effect arising from the enhanced spatial electric field and metal protection introduced by C–Cl bond formation (Fig. 6c).

3 Conclusions

In conclusion, our study has revealed the corrosion-resistance mechanism of a non-noble metal-based dual-protection hetero-interface catalyst in seawater reduction reactions. By constructing heterointerfaces and introducing dopant groups with strong electronic interactions, an enhanced spatial electric field can be generated. This field can accelerate interface electron transfer, thereby inducing partial electron enrichment at the NG surface and suppressing Cl⁻ diffusion. Additionally, we find that due to the formation of C–Cl bonds on the graphene surface, strong repulsion against Cl⁻ ions were further achieved. By integrating the two key factors for Cl⁻ resistance, i.e., electric field and steric effect, the NG/NiMo dual-protection heterointerface achieves not only long-term durability but also Pt/C-comparable activity for seawater electrolysis. The NG/NiMo-assembled AEM electrolyzer

achieved ampere-level current densities at a low cell voltage of 1.86 V and retained over 95% of its initial current density during a 300 h continuous test. This study offers innovative insights for the development of corrosion-proof metal catalysts for applications under seawater conditions.

Author contributions

Yue Xu, Yingjian He, Shuaidong Li, and Shanling Li contributed equally to this work. Kailong Hu conceived this project and designed the experiments. Yingjian He and Yue Xu performed the electrochemical experiments. Shuaidong Li conducted the DFT calculations. Junqin Shi and Shanling Li led the MD simulations. Yingjian He and Yue Xu performed the microscopy analysis and conducted the AEM cell experiments. Yingjian He contributed to the sample preparations. Yingjian He, Shuai-dong Li, Yue Xu, Zeyun Cai, Junqin Shi, Shanling Li, Xi Lin, and Kailong Hu analyzed the experimental data. Yue Xu, Yingjian He, Shuaidong Li, Junqin Shi, Shanling Li, and Kailong Hu wrote and revised the manuscript.

Conflicts of interest

The authors declare no conflict of interest.

Data availability

The data supporting this article have been included as part of the supplementary information (SI). Supplementary informa-tion: additional experimental details and materials character-ization data. See DOI: https://doi.org/10.1039/d5sc08327c.

Acknowledgements

References

1 Y. Yang, L. Tong, S. Yin, Y. Liu, L. Wang, Y. Qiu and Y. Ding, *J. Cleaner Prod.*, 2022, **376**, 134347.

2 X. Yang, C. P. Nielsen, S. Song and M. B. McElroy, *Nat. Energy*, 2022, **7**, 955–965.

3 H. Kojima, K. Nagasawa, N. Todoroki, Y. Ito, T. Matsui and R. Nakajima, *Int. J. Hydrogen Energy*, 2023, **48**, 4572–4593.

4 S. Dresp, F. Dionigi, M. Klingenhof and P. Strasser, *ACS Energy Lett.*, 2019, **4**, 933–942.

5 Z. Yu and L. Liu, *Adv. Mater.*, 2024, **36**, 2308647.

6 F. Sun, J. Qin, Z. Wang, M. Yu, X. Wu, X. Sun and J. Qiu, *Nat. Commun.*, 2021, **12**, 4182.

7 O. Fahad Aldosari, I. Hussain and Z. Malaibari, *J. Energy Chem.*, 2023, **80**, 658–688.

8 W. Liu, J. Yu, T. Li, S. Li, B. Ding, X. Guo, A. Cao, Q. Sha, D. Zhou, Y. Kuang and X. Sun, *Nat. Commun.*, 2024, **15**, 4712.

9 X. Xu, Y. Lu, J. Shi, X. Hao, Z. Ma, K. Yang, T. Zhang, C. Li, D. Zhang, X. Huang and Y. He, *Nat. Commun.*, 2023, **14**, 7708.

10 Y. Kuang, M. J. Kenney, Y. Meng, W.-H. Hung, Y. Liu, J. E. Huang, R. Prasanna, P. Li, Y. Li, L. Wang, M.-C. Lin, M. D. McGehee, X. Sun and H. Dai, *Proc. Natl. Acad. Sci. U. S. A.*, 2019, **116**, 6624–6629.

11 S. Zhang, W. Xu, H. Chen, Q. Yang, H. Liu, S. Bao, Z. Tian, E. Slavcheva and Z. Lu, *Adv. Mater.*, 2024, **36**, 2311322.

12 W. He, X. Li, C. Tang, S. Zhou, X. Lu, W. Li, X. Li, X. Zeng, P. Dong, Y. Zhang and Q. Zhang, *ACS Nano*, 2023, **17**, 22227–22239.

13 Z. Wu, Y. He, S. Wang, S. Li, Z. Zhang, B. Zhou, Y. Xu, Z. Jiang, J. Chen, Y. Chen, Z. Cai, X. Lin and K. Hu, *J. Power Sources*, 2025, **648**, 237372.

14 S. Li, Y. Xu, X. Zhou, J. Li, S. Wang, Y. Chen, J. Chen, Z. Jiang, Y. Hao, K. Li, Z. Cai and K. Hu, *J. Energy Chem.*, 2026, **113**, 482.

15 S. Zhang, Y. Wang, S. Li, Z. Wang, H. Chen, L. Yi, X. Chen, Q. Yang, W. Xu, A. Wang and Z. Lu, *Nat. Commun.*, 2023, **14**, 4822.

16 Y. Liu, Y. Wang, P. Fornasiero, G. Tian, P. Strasser and X.-Y. Yang, *Angew. Chem., Int. Ed.*, 2024, **63**, e202412087.

17 D. Zhang, H. Cheng, X. Hao, Q. Sun, T. Zhang, X. Xu, Z. Ma, T. Yang, J. Ding, X. Liu, M. Yang and X. Huang, *ACS Catal.*, 2023, **13**, 15581–15590.

18 Y. Xu, S. Li, J. Cao, Z. Ren, Y. He, Z. Cai, C. Hou, J. Zhang, Z. Chen, R. Shi, S. Jeong, X. Lin and K. Hu, *Energy Environ. Sci.*, 2025, **18**, 4811–4820.

19 Q. Xu, J. Zhang, H. Zhang, L. Zhang, L. Chen, Y. Hu, H. Jiang and C. Li, *Energy Environ. Sci.*, 2021, **14**, 5228–5259.

20 H. Jin, J. Xu, H. Liu, H. Shen, H. Yu, M. Jaroniec, Y. Zheng and S.-Z. Qiao, *Sci. Adv.*, 2023, **9**, adi7755.

21 A. A. Bhardwaj, J. G. Vos, M. E. S. Beatty, A. F. Baxter, M. T. M. Koper, N. Y. Yip and D. V. Esposito, *ACS Catal.*, 2021, **11**, 1316–1330.

22 L. Shao, X. Han, L. Shi, T. Wang, Y. Zhang, Z. Jiang, Z. Yin, X. Zheng, J. Li, X. Han and Y. Deng, *Adv. Energy Mater.*, 2024, **14**, 2303261.

23 P. Li, S. Zhao, Y. Huang, Q. Huang, B. Xi, X. An and S. Xiong, *Adv. Energy Mater.*, 2024, **14**, 2303360.

24 Y. Xu, Y. He, S. Wang, Z. Wu, H. Hu, S. Jeong, X. Lin and K. Hu, *Chem. Phys. Rev.*, 2023, **4**, 041312.

25 X. Kang, F. Yang, Z. Zhang, H. Liu, S. Ge, S. Hu, S. Li, Y. Luo, Q. Yu, Z. Liu, Q. Wang, W. Ren, C. Sun, H.-M. Cheng and B. Liu, *Nat. Commun.*, 2023, **14**, 3607.

26 J. Peng, Z. Zhang, H. Wang, P. Zhang, X. Zhao, Y. Jia, Y. Yue and N. Li, *Small*, 2024, **20**, 2308528.

27 K. Hu, S. Jeong, M. Wakisaka, J.-i. Fujita and Y. Ito, *Metals*, 2018, **8**, 83.

28 K. Hu, T. Ohto, L. Chen, J. Han, M. Wakisaka, Y. Nagata, J.-i. Fujita and Y. Ito, *ACS Energy Lett.*, 2018, **3**, 1539–1544.

29 Y. Xu, S. Li, Y. He, F. Shiokawa, S. Jeong, A. A. H. Tajuddin, Z. Xi, Y. Ito, J. Zhang, Z. Cai, X. Lin and K. Hu, *J. Energy Chem.*, 2025, **103**, 344–352.

30 S. Feng, M. C. dos Santos, B. R. Carvalho, R. Lv, Q. Li, K. Fujisawa, A. L. Elias, Y. Lei, N. Perea-Lopez, M. Endo, M. Pan, M. A. Pimenta and M. Terrones, *Sci. Adv.*, 2016, **2**, e1600322.

31 J. Zhang, T. Wang, P. Liu, Z. Liao, S. Liu, X. Zhuang, M. Chen, E. Zschech and X. Feng, *Nat. Commun.*, 2017, **8**, 15437.

32 A. A. H. Tajuddin, G. Elumalai, Z. Xi, K. Hu, S. Jeong, K. Nagasawa, J.-i. Fujita, Y. Sone and Y. Ito, *Int. J. Hydrogen Energy*, 2021, **46**, 38603–38611.

33 K. Hu, M. Wu, S. Hinokuma, T. Ohto, M. Wakisaka, J.-i. Fujita and Y. Ito, *J. Mater. Chem. A*, 2019, **7**, 2156–2164.

34 K. Hu, X. Wang, Y. Hu, H. Hu, X. Lin, K. M. Reddy, M. Luo, H.-J. Qiu and X. Lin, *ACS Nano*, 2022, **16**, 19165–19173.

35 Y. Huang, J. Ge, J. Hu, J. Zhang, J. Hao and Y. Wei, *Adv. Energy Mater.*, 2018, **8**, 1701601.

36 H. Hu, Y. Wang, Y. Xu, L. Jin, S. Jeong, X. Xie, C. Xiong, B. Zhou, W. Sun, J. Zhang, X. Lin and K. Hu, *Chem. Eng. J.*, 2024, **492**, 152325.

37 K. Hu, T. Yu, Y. Zhang, X. Lin, Y. Zhao, G. Xie, X. Liu, X. Lin, J. i. Fujita, H.-J. Qiu and Y. Ito, *Adv. Funct. Mater.*, 2021, **31**, 2103632.

38 W. Xu, Z. Wang, P. Liu, X. Tang, S. Zhang, H. Chen, Q. Yang, X. Chen, Z. Tian, S. Dai, L. Chen and Z. Lu, *Adv. Mater.*, 2024, **36**, 2306062.

39 J. Guo, Y. Zheng, Z. Hu, C. Zheng, J. Mao, K. Du, M. Jaroniec, S.-Z. Qiao and T. Ling, *Nat. Energy*, 2023, **8**, 264–272.

40 N. Wang, P. Ou, S.-F. Hung, J. E. Huang, A. Ozden, J. Abed, I. Grigioni, C. Chen, R. K. Miao, Y. Yan, J. Zhang, Z. Wang, R. Dorakhan, A. Badreldin, A. Abdel-Wahab, D. Sinton, Y. Liu, H. Liang and E. H. Sargent, *Adv. Mater.*, 2023, **35**, 2210057.

41 S. Zhao, Y. Wang, Y. Hao, L. Yin, C.-H. Kuo, H.-Y. Chen, L. Li and S. Peng, *Adv. Mater.*, 2024, **36**, 2308925.

42 J. Chang, G. Wang, Z. Yang, B. Li, Q. Wang, R. Kuliiev, N. Orlovskaya, M. Gu, Y. Du, G. Wang and Y. Yang, *Adv. Mater.*, 2021, **33**, 2101425.

43 H. Shi, T. Wang, J. Liu, W. Chen, S. Li, J. Liang, S. Liu, X. Liu, Z. Cai, C. Wang, D. Su, Y. Huang, L. Elbaz and Q. Li, *Nat. Commun.*, 2023, **14**, 3934.

44 A. E. Tonelli and T. N. Bowmer, *J. Polym. Sci., Part B: Polym. Phys.*, 1987, **25**, 1153–1156.

45 Z. Kou, B. Guo, Y. Zhao, S. Huang, T. Meng, J. Zhang, W. Li, I. S. Amiinu, Z. Pu, M. Wang, M. Jiang, X. Liu, Y. Tang and S. Mu, *ACS Appl. Mater. Interfaces*, 2017, **9**, 3012–3712.

46 M. Schorr, B. S. Valdez, M. S. Stoytcheva and R. K. Zlatev, *ECS Trans.*, 2008, **13**, 143.

47 A. G. Oshchepkov, A. Bonnefont, V. N. Parmon and E. R. Savinova, *Electrochim. Acta*, 2018, **269**, 111–118.

48 Y. Sui, Z. Zhuo, M. Lei, L. Wang, M. Yu, A. M. Scida, S. K. Sandstrom, W. Stickle, T. D. O'Larey, D.-e. Jiang, W. Yang and X. Ji, *Adv. Mater.*, 2023, **35**, 2302595.